



# Influence of thermomechanical processing parameters on microstructural evolution of a gamma-prime strengthened cobalt based superalloy during high temperature deformation

Nithin Baler<sup>a</sup>, Prafull Pandey<sup>b</sup>, Kamanio Chattopadhyay<sup>b</sup>, Gandham Phanikumar<sup>a,\*</sup>

<sup>a</sup> Department of Metallurgical and Materials Engineering, Indian Institute of Technology Madras, Chennai, 600036, India

<sup>b</sup> Department of Materials Engineering, Indian Institute of Science, Bangalore, 560012, India



## ARTICLE INFO

### Keywords:

Cobalt base superalloy  
Strain rate sensitivity  
Dynamic recrystallization  
Thermo mechanical processing

## ABSTRACT

Recent reports on  $\gamma'$ -L1<sub>2</sub> strengthened cobalt base superalloys showed the potential of this class of alloys to replace nickel-base superalloys for high-temperature applications. The studies on thermo-mechanical processing behavior of these new class of alloys are limited. Thus, the present study investigates the thermo-mechanical processing behavior of Co-30Ni-10Al-2Nb-4Ti-12Cr (all in at. %, referred to as Co10Al2Nb)  $\gamma'$  strengthened cobalt base superalloy at different conditions of temperature and strain rates. The high temperature uniaxial compression tests were carried out using Gleeble 3800® in the temperature range of 1298–1448 K and the strain rate range of 0.001 to 10 s<sup>-1</sup>. The flow curves exhibited three distinct flow behavior characteristics: work hardening, softening, and steady state. Microstructures of deformed samples revealed the presence of fine strain-free dynamic recrystallization (DRX) grains in lower strain rate regime (0.001 to 0.1 s<sup>-1</sup>) and flow localization features like shear bands, cracks along the grain boundary in high strain rate regime (especially at 10 s<sup>-1</sup>) for all the temperatures. The strain rate sensitivity (m) map along with instability ( $\xi(\dot{\varepsilon})$ ) map revealed two distinct domains, one with  $m \sim 0.15$  to 0.3 (0.001 to 1 s<sup>-1</sup>), and other domain with  $m < 0.13 (>1$  s<sup>-1</sup>) for the temperature range studied. DRX was observed to be the main restoration process at  $m \sim 0.15$  to 0.3, whereas the flow localization was dominant at  $m < 0.13$ . The microstructure at different strain levels revealed that discontinuous dynamic recrystallization (DDRX) was the prevalent deformation mechanism for the present alloy. The strain field distribution obtained from the FEM simulation for different deformation conditions correlated with DRX microstructure evolution was also presented.

## 1. Introduction

The  $\gamma/\gamma'$  strengthened nickel base superalloys are employed in the manufacturing of most of the parts in gas turbine engine [1]. The presence of  $\gamma'$  L1<sub>2</sub> ordered coherent precipitates provides the required properties in nickel base superalloys at high temperature ( $>1073$  K) [2]. However, at present with the advancement of technology and a desire to increase efficiency, the temperature in the turbine engines is increasing steadily. Thus, the working environment in the turbines is fast reaching the limit of capability of nickel base superalloys. In order to accommodate the increase in temperature, there are a lot of studies that are going on in the area of high temperature materials alternative to nickel base superalloys [3]. Cobalt base superalloys are one such high temperature materials that have a potential to replace the conventional nickel base

superalloys in some parts in gas turbine engines [4,5]. Recent research on high temperature properties on  $\gamma'$  strengthened cobalt base superalloys that exhibits properties comparable and higher than the 1st generation nickel base superalloys [6–8]. In addition to high temperature properties,  $\gamma'$  strengthened cobalt base superalloys shows higher solidus and liquidus temperatures (50 to 100 °C), less segregation during solidification, and better sulfidation resistance than nickel base superalloys [9–11].

Most of the gas turbine engine parts are manufactured in either cast or wrought form. The turbine engine blades and vanes are usually produced by casting routes to provide a higher creep resistance at high temperatures. On the other hand, turbine discs and shafts are produced by wrought form, to provide higher tensile strength and low cycle fatigue resistance [12]. The wrought form involves the thermomechanical

\* Corresponding author.

E-mail address: [gphani@iitm.ac.in](mailto:gphani@iitm.ac.in) (G. Phanikumar).

processing of cast ingots, which involves breaking of dendrites, removing the segregation and formation of new grains. The formation of new grains mainly depends on the restoration processes operating during high temperature deformation.

The hot deformation behavior and microstructure evolution of nickel base superalloys are extensively studied [13–16]. Most of these studies reported dynamic recrystallization (DRX) is the dominant restoration process that occurs during the high temperature deformation. There are few reports available on hot deformation behavior and associated dynamic recrystallization (DRX) mechanism of various cobalt based alloys. The influence of different temperatures and strain rates on the microstructural evolution of the Co20Cr15W10Ni cobalt base superalloy has been investigated [17]. It is observed that dynamic recrystallization (DRX) is the major softening mechanism, where dynamic recrystallization (DRX) grains nucleate along the original grain boundaries. Favre et al. [18] reported that during high temperature deformation, the nucleation of dynamic recrystallization (DRX) grains in L-605 cobalt based alloys is a result of the bulging of original boundaries. Yamanaka et al. [19,20] reported the formation of ultra-fine grains in Co–28Cr–9W–1Si–0.05C cobalt base alloy is mainly due to the dynamic recrystallization (DRX) restoration process nucleated along the pre-existing grain boundaries.

The introduction of  $\gamma'$  precipitates in Co–Al–W, and Co–Al–Mo–Nb/Ta system, and subsequent research on these alloys showed the high temperature properties are similar to nickel based superalloys [21–26]. The majority of the research in Co–Al–W alloys has been carried out in cast alloys [27–34]. Studies on the wrought form or thermomechanical processing behavior of Co-based superalloy are limited. Neumaier et al. [35,36] have reported the  $\gamma'$  strengthened CoAlW alloy produced in wrought form exhibited a better creep and oxidation resistance compared to Udimet 720Li® and waspaloy®. McDevitt has demonstrated the ingot metallurgy route for the production of cast and wrought form of  $\gamma'$  strengthened cobalt base superalloys [37]. Recently, the influence of different temperature and strain rate on the microstructure evolution of Co–9.8Al–7.4W–2.7Ti–20.4Ni–0.4C–0.1B (at.%)  $\gamma'$  strengthened cobalt based superalloy has been investigated by Sani et al. [38]. They have reported that discontinuous dynamic recrystallization (DDRX) is a major restoration mechanism.

In Co–Al–Mo–Nb/Ta base alloy, Makineni et al. showed uniform distribution of the  $\text{Co}_3(\text{Al}, \text{Mo}, \text{Nb}/\text{Ta})\text{L1}_2$  ordered  $\gamma'$  precipitates in the FCC cobalt matrix [5]. The reported cuboidal  $\gamma/\gamma'$  microstructure is akin to conventional nickel base superalloys. However, these alloys suffer from lack of thermal stability due to lower solvus temperature [39]. In order to improve the solvus temperature, long term stability, and high temperature properties, alloying addition such as Ni, Ti, Re, Cr, and W was made to base Co–10Al–5Mo–2Nb/Ta alloy [24,26,40–44]. The studies have shown that these alloys exhibit higher solvus temperature and comparable high temperature properties with some of nickel base superalloys. The most of the research in this class of alloys (including Co–Al–W) was focused more on improving the solvus temperature through alloying addition, high temperature stability, high temperature properties, and behavior of these alloys under different environments. The thermomechanical processing of this class of alloys (including Co–Al–W alloys) is not explored in detail [45].

In the present study, the high temperature deformation behavior of newly developed Co–30Ni–10Al–2Nb–4Ti–12Cr (all in at. %, referred to as Co10Al2Nb)  $\gamma'$  strengthened cobalt base superalloy were studied. The present alloy exhibit a higher solvus temperature of 1362 K, and low density of  $7.84 \text{ g cm}^{-3}$  [46,47]. The uniaxial compression tests were carried out at different combinations of temperatures and strain rates. The different thermomechanical parameters were used to simulate the experimental processing conditions for newly developed  $\gamma'$  strengthened cobalt base superalloy. The deformation mechanisms were identified from flow curves and validated with the microstructure evolution of the deformed samples, and strain rate sensitivity (m) map. The degree of deformation was varied by controlling the amount of strain given to the

**Table 1**

Nominal and measured composition (in atomic %) of studied alloy as measured by energy dispersive X-ray spectroscopy (EDS) in scanning electron microscopy (SEM).

Nomenclature	Nominal Composition	Measured Composition
Co10Al2Nb	Co–30Ni–10Al–2Nb–4Ti–12Cr	Co–29.5±0.2Ni–9.6±0.2Al–1.9±0.1Nb–4.5±0.1Ti–12.7±0.3Cr

sample to identify the associated restoration process. The detailed microstructure characterization was carried out using optical microscopy (OM), scanning electron microscope-electron backscattered diffraction (SEM-EBSD), and transmission electron microscope (TEM). Finite element method (FEM) simulations were performed for the experimentally studied deformation conditions. The strain field distribution obtained using Finite element method (FEM) simulations was correlated with dynamic recrystallization (DRX) microstructural evolution in detail.

## 2. Materials and methods

### 2.1. Alloy preparation

**Table 1** shows the nominal and measured composition (at. %) of the cobalt base superalloy used for this study. All the elements used for the preparation of the alloy were 99.99 % pure and melted and cast in the form of buttons in a vacuum arc-melting unit. A tungsten electrode and a water-cooled copper hearth were used for arc melting in a partial argon atmosphere. The button was repeatedly melted for 6–8 times by flipping after each melting to achieve a homogeneous distribution of alloying elements. The alloy button was then cast in the form of a cylindrical rod ( $\phi$  6 mm in diameter and 70 mm in height) using a water-cooled split copper mould in a vacuum suction casting unit under a partial argon atmosphere. The cast rods were solutionized at 1443 K for 15 h in a tube furnace operating under a vacuum of  $10^{-5}$  Pa followed by argon quenching. The composition of the solution treated sample was measured using scanning electron microscope (SEM)-energy dispersive X-ray spectroscopy (EDS), and it is given in **Table 1**.

### 2.2. Hot compression tests

The standard compression samples with a diameter and height of 6 and 9 mm (aspect ratio 1:1.5), respectively, were cut from the solution treated cast rods using wire electrical discharge machining (EDM). Isothermal uniaxial compression tests were carried out at temperatures of 1298, 1348, 1398, and 1448 K and strain rates of 0.001, 0.01, 0.1, 1, and  $10 \text{ s}^{-1}$  in a thermomechanical simulator (Gleeble 3800®). A combination of nickel paste and graphite foils was used as a lubricant between the tungsten carbide anvil and the sample to minimize the frictional effect. A K-type thermocouple was spot welded to the sample to control the temperature. All the specimens were heated to the test temperature at a heating rate of  $5 \text{ K s}^{-1}$  and soaked for 300 s to achieve a uniform temperature throughout the sample. Samples were water quenched immediately after reaching a true strain of 0.7 (50 % deformation). Here, the water quenching was done mainly to arrest the deformed microstructure. The deformed samples were cut at the centre parallel to the compression axis for microstructural characterization.

### 2.3. Microstructure characterization

The microstructure of the deformed samples was characterized using an optical microscope, scanning electron microscope-electron backscattered diffraction (SEM-EBSD), and transmission electron microscope (TEM). The longitudinal section of the deformed samples was polished using 800 to 3000 grit Silicon Carbide papers. The final polishing was

carried out using a 3 to 0.5-μm size diamond paste. The polished samples were etched using Marble's reagent (20 mL HCl, 20 mL distilled water, and 4 g CuSO<sub>4</sub>) for 240 s and observed under the optical microscope. Selected samples were prepared for electron backscattered diffraction (EBSD) characterization. The standard metallographic polishing technique was followed for EBSD sample preparation. The electro polishing was carried out using a Struers Lectropol-5® electro polishing machine using a standard A2 solution. The electron backscattered diffraction (EBSD) scans were performed with a step size of 1 μm in FIB (Helios G4 UX®) equipped with an electron backscattered diffraction (EBSD) detector. TSL-OIM® software (version 7.3) was used to analyze the data obtained from the electron backscattered diffraction (EBSD) scan. A transmission electron microscope (TEM) (Tecnai T20), operating at 200 kV was used to characterize the dynamic recrystallization (DRX) grains in deformed samples. For transmission electron microscope (TEM) analysis, the deformed samples were polished up to 100 μm thickness using emery paper followed by punching to 3 mm diameter discs. The discs were then thinned down to 40 μm using fine emery paper. The final thinning down to <150 nm (electron transparent) was done in argon ion milling (Gatan PIPS®) operating at an accelerating voltage of 5 kV and 5° incident angle.

#### 2.4. Grain orientation spread (GOS)

Grain orientation spread (GOS) criteria was employed to separate the recrystallized grains from deformed grains in the inverse pole figure (IPF) map. Grain orientation spread (GOS) is calculated by averaging the orientation change between each pixel in a given grain and the average orientation of that grain. Large orientation change in the deformed grains due to a higher degree of accumulation of dislocation leads to a higher Grain orientation spread (GOS) value, whereas the dynamic recrystallization (DRX)/strain-free grain will have lesser Grain orientation spread (GOS) value. In the present study, the Grain orientation spread (GOS) cut off < 2° is used to separate recrystallized grains from deformed grains.

#### 2.5. Local misorientation

Kernel Average Misorientation (KAM) map was used to measure the local misorientation changes in the deformed samples. Kernel Average Misorientation (KAM) map is based on the average orientation changes between each kernel, and it's nearest neighbouring kernels, except those kernels which are having orientation changes > 5°. Kernel Average Misorientation (KAM) value also gives an approximation of the dislocation accumulation and restoration process in a deformed material.

#### 2.6. Finite element method (FEM) simulation

The uniaxial hot compression tests were simulated by using a commercial Finite element method (FEM) based software (SIMUFACT®) using an upsetting module with a hydraulic press. Here, the average strain rate was controlled by controlling stroke velocity and deformation time (s). A quadrilateral element with a size of 0.025 mm, 42840 elements, and 2D-axisymmetric conditions were used for simulation. The flow curves obtained from the hot compression tests at different deformation conditions were used as an input to the material database for Finite element method (FEM) simulation. Thermo-physical material properties required for simulation were measured using differential scanning calorimeter (DSC). An optimum frictional factor of 0.5 was used for the frictional condition between the die and material. The boundary conditions were kept in such a way that to attain the isothermal condition by keeping the convective heat transfer and radiative effects from the sample as low as possible. The strain field distribution at different locations during the deformation was used to explain the inhomogeneity in recrystallization behavior in detail.

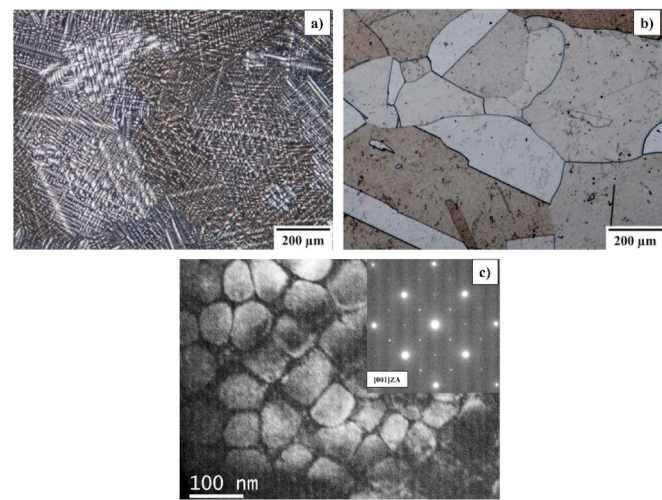


**Fig. 1.** (a&b) optical micrograph of Co10Al2Nb alloy: a) as cast microstructure, b) after solution treatment at 1443 K for 15 h followed by Ar quenching, c) dark field image was taken in [001] zone axis after subjecting solution treatment revealing fine γ' precipitates in γ matrix.

### 3. Results

#### 3.1. Microstructure

**Fig. 1** shows the as-cast and solutionized microstructures of the Co10Al2Nb alloy. Typical dendritic structure with the segregation of alloying elements along the interdendritic regions was observed in the as-cast sample (**Fig. 1(a)**). The coarse grains with annealing twins can be observed in the solutionized sample (**Fig. 1(b)**). The average grain size of the solutionized sample was around 450±50 μm. **Fig. 1(c)** shows the presence of fine γ' precipitates with an average size of 75±5 nm in the solutionized sample.

#### 3.2. Flow behavior

**Fig. 2** shows the true stress-true strain curves of the Co10Al2Nb alloy deformed in the temperature range of 1298–1448 K and the strain rate range of 0.001–10 s<sup>-1</sup>. The flow curves exhibited an initial work hardening followed by softening and/or steady-state depending on the temperature and strain rate. At a strain rate >1 s<sup>-1</sup>, after work hardening flow stress decreases continuously with strain, whereas at a strain rate <1 s<sup>-1</sup> softening and steady-state can be observed at all temperatures. The variation of the flow stress with respect to temperature and strain rate is shown in **Fig. 3**. It was observed that there is a strong dependence of flow stress value on the temperature and strain rate. The value of flow stress increases with the increase in strain rate (**Fig. 3(a)**) and decreases with an increase in temperature for all the strain (**Fig. 3(b)**).

#### 3.3. Strain rate sensitivity

The strain rate sensitivity (m) values for different deformation conditions were calculated by using the following equation [48].

$$m = \frac{\partial \ln \sigma}{\partial \ln \dot{\epsilon}} \quad [1]$$

In this study, the flow stress value at 0.65 true strain at different conditions of temperature and strain rate was used to calculate the strain rate sensitivity parameter (m). The flow stress value at different strain rates was interpolated to finely spaced data by using a cubic spline function. The m value was then calculated, and which is equal to the first derivative of the cubic spline fit. **Fig. 4** shows the iso-strain rate sensitivity contour map generated at 0.65 strain in the logarithmic strain rate

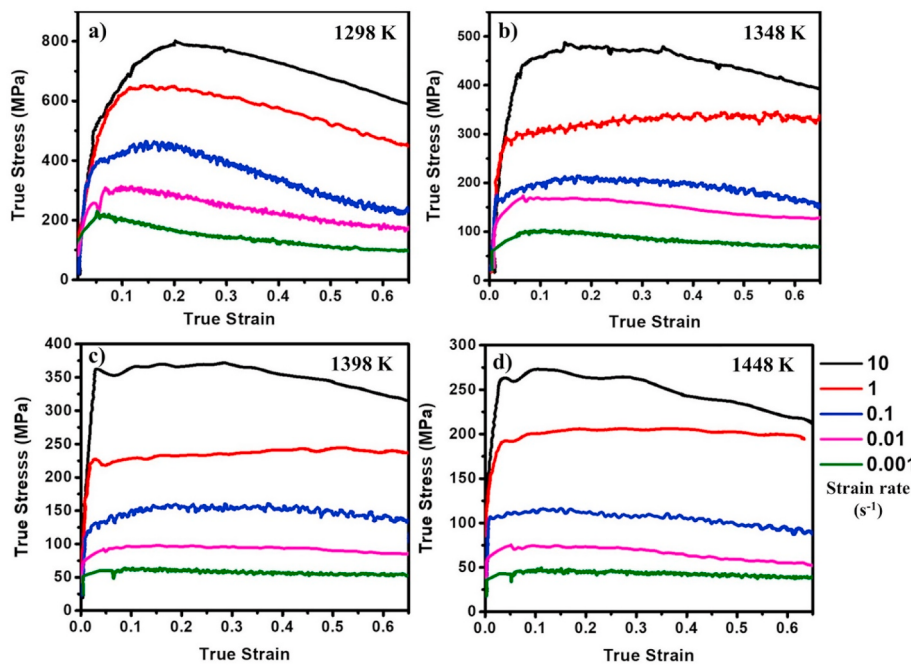


**Fig. 2.** True stress-strain curves obtained at different temperatures and strain rate a) 1298 K, b) 1348 K, c) 1398 K, and d) 1448 K.

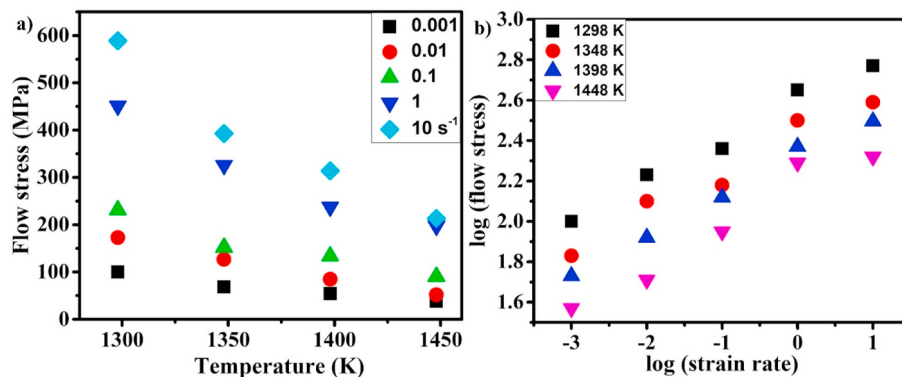


**Fig. 3.** (a,&b) Dependence of flow stress with temperature and strain rate at 0.65 strain.

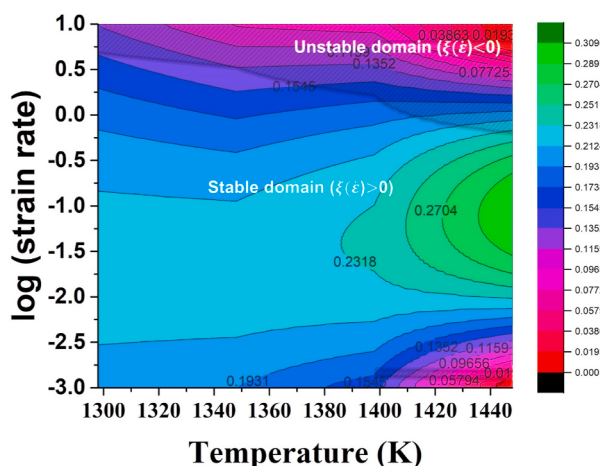


**Fig. 4.** Strain rate sensitivity (m) contour map plotted considering stress value at 0.65 true strain. Instability regions are shaded in the map.

vs. temperature scale. The contours represent the strain rate sensitivity ( $m$ ) value, which varies from 0.01 to 0.3 depending on the deformation condition. Strain rate sensitivity map reveals the two domains. The first domain with  $m$  value  $< 0.13$ , and at strain rate  $> 1 \text{ s}^{-1}$ . The other domain, where the  $m$  value varies from 0.15 to 0.3, and a strain rate of 0.001 to  $0.1 \text{ s}^{-1}$ . Since the obtained  $m$  values at different deformation conditions for the present alloy is greater than zero ( $m > 0$ ), the deformed sample is not expected to show flow instability. Generally a higher  $m$  value domain is considered safe for hot working. However, at strain rate near to  $10 \text{ s}^{-1}$ , the  $m$  value is close to zero, there may be possibility occurrence of flow instability. The strain rate sensitivity map alone is not sufficient to differentiate safe and unsafe hot working domain. The instability criterion developed by Ziegler was used in the present study to identify the flow instability during hot deformation [49], which is given by the following equation

$$\xi(\dot{\epsilon}) = \frac{\partial \ln \left[ \frac{m}{(m+1)} \right]}{\partial \ln \dot{\epsilon}} + m < 0 \quad [2]$$

The deformation condition satisfy the above condition are consider to be unsafe for hot working. The unsafe domain ( $(\xi(\dot{\epsilon}) < 0)$ ) are represented in a hashed lines on the strain rate sensitivity map (Fig. 4).



**Fig. 5.** (a–t) Optical micrograph of Co10Al2Nb alloy deformed to a 0.7 true strain followed by water quenching at different temperatures and strain rates.

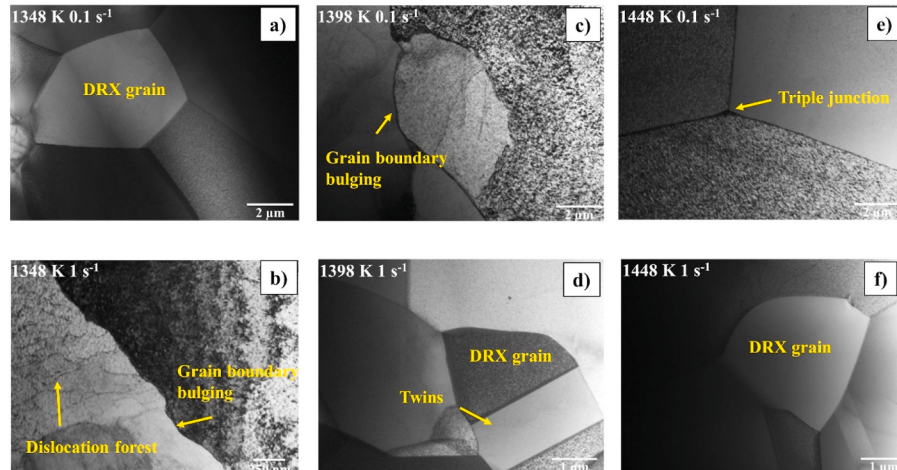


**Fig. 6.** TEM bright field images of deformed sample at different temperature and strain rate, a, & b) deformed at strain rate of 0.1 and 1 s<sup>-1</sup>, and at temperature 1348 K, c, & d) deformed at strain rate of 0.1 and 1 s<sup>-1</sup>, and at temperature 1398 K, and e, & f) deformed at strain rate of 0.1 and 1 s<sup>-1</sup>, and at temperature 1448 K.

#### 3.4. Microstructural characterization of deformed samples

Fig. 5(a–t) shows the optical microstructures of deformed samples at different temperatures and strain rates. Deformation at a strain rate of 0.001 s<sup>-1</sup> for all temperatures (except 1298 K) exhibited a fully recrystallized microstructure, and the dynamic recrystallization (DRX) grain size increased with an increase in deformation temperature as shown in Fig. 5(a, f, & k). At a strain rate of 0.01–1 s<sup>-1</sup>, microstructures consisted of partially recrystallized grains, as shown in Fig. 5(b–d, g–i, & l–n) for all deformation temperatures (except for 1298 K). Here, the dynamic recrystallization (DRX) area fraction and size decrease with an increase in strain rates and increase with the increase in temperature. At a strain rate of 10 s<sup>-1</sup> and for all test temperatures, microstructure revealed flow

instability features like grain boundary cracking, shear bands, and cavities, as shown in Fig. 5(e, j, o, & t). At 1298 K, and a strain rate of 0.001 s<sup>-1</sup>, the sample exhibited a partially recrystallized microstructure (Fig. 5p). As the strain rate increased further (0.01 s<sup>-1</sup>), the partial recrystallized microstructure consisted of fine dynamic recrystallization (DRX) grains and deformed grains (Fig. 5q). At a strain rate of 0.1 s<sup>-1</sup>, microstructure mostly showed deformed grains and finer DRX grains along the grain boundary, as shown in Fig. 5(r). In Fig. 5(s) microstructure consisted of deformed original grains, and no sign of dynamic recrystallization (DRX) activity was observed at a strain rate of 1 s<sup>-1</sup>.

Fig. 6 shows the TEM micrograph of deformed samples at different temperature and strain rate conditions. At 1348 K and strain rate of 0.1 s<sup>-1</sup>, the presence of new strain-free DRX grains was observed shown in

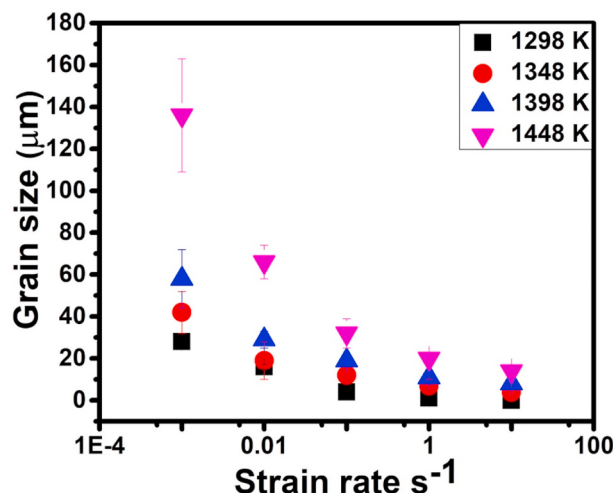


**Fig. 7.** Dynamic recrystallization (DRX) grain size evolution at different temperature and strain rate.

**Fig. 6(a).** At 1348, 1398 K, and a strain rate of 0.1 and  $1 \text{ s}^{-1}$ , microstructure consisted of features such as grain boundary bulging and dislocation forest (Fig. 6(b, & c)). Fig. 6(d) shows the formation of new strain-free dynamic recrystallization (DRX) grains along with twins at 1398 K and a strain rate of  $1 \text{ s}^{-1}$ . Deformation at 1348 K, and strain rate of 0.1, and  $1 \text{ s}^{-1}$ , dynamic recrystallization (DRX) grain formation at the triple junction was revealed (Fig. 6(e & f)). In addition, the variation of dynamic recrystallization (DRX) grain size at different conditions was measured using the linear intercept method and plotted as shown in Fig. 7. It is observed that the dynamic recrystallization (DRX) grain size increases with an increase in temperature, and increases with a decrease in strain rate.

### 3.5. Effect of deformation parameter on microstructure evolution

#### 3.5.1. Effect of strain rate on microstructure evolution

The effect of strain rate on the evolution of the dynamic recrystal-

lization (DRX) microstructure was studied by deforming samples to a true strain of 0.7 at a constant temperature of 1348 K and at a strain rate of  $0.001\text{--}10 \text{ s}^{-1}$ . The IPF map of deformed samples at different strain rates is shown in Fig. 8. At lowest strain rate ( $0.001 \text{ s}^{-1}$ ) deformed sample exhibited a fully recrystallized microstructure consisted of fine dynamic recrystallization (DRX) grains and annealing twins ( $\Sigma 3$  boundaries), as shown in Fig. 8(a). As the strain rates increased further to  $0.01 \text{ s}^{-1}$ ,  $0.1 \text{ s}^{-1}$ , and  $1 \text{ s}^{-1}$ , deformed samples exhibited a typical necklace type of structure (partial recrystallized) with a decrease in the fraction of dynamic recrystallization (DRX) grains and annealing twins ( $\Sigma 3$  boundaries) shown in Fig. 8 (b, c, & d). At the highest strain rate of  $10 \text{ s}^{-1}$ , the microstructure consisted mostly of deformed grains (Fig. 8(e)). The plot is shown in Fig. 8, illustrates the variation of dynamic recrystallization (DRX) grain size ( $\mu\text{m}$ ), twin boundary ( $\Sigma 3$  boundaries) fraction (%), and dynamic recrystallization (DRX) area fraction (%) at different strain rates ( $\text{s}^{-1}$ ). The complete recrystallized microstructure with dynamic recrystallization (DRX) fraction of 98.5 %, dynamic recrystallization (DRX) grain size of  $42 \pm 15 \mu\text{m}$ , and twin boundary ( $\Sigma 3$  boundaries) fraction of 40.5 % can be observed in the sample deformed at the lowest strain rate of  $0.001 \text{ s}^{-1}$ . At strain rate  $0.01 \text{ s}^{-1}$ , the dynamic recrystallization (DRX) fraction, grain size, and twin boundary ( $\Sigma 3$  boundaries) fraction reduced to 88.7 %,  $19 \pm 9 \mu\text{m}$  and 37 %, respectively. With a further increase in the strain rate of  $0.1 \text{ s}^{-1}$ , DRX grains with a size of  $13 \pm 2 \mu\text{m}$ , the area fraction of 42 %, and twin boundary ( $\Sigma 3$  boundaries) fraction of 22 % were observed. At a strain rate of  $1 \text{ s}^{-1}$ , fine dynamic recrystallization (DRX) grains with size  $7 \pm 3 \mu\text{m}$ , and fraction 36 %, and twin boundary ( $\Sigma 3$  boundaries) fraction of 16 % was observed. There is no sign of dynamic recrystallization (DRX) grains evolution at a strain rate of  $10 \text{ s}^{-1}$  as shown in the inverse pole figure (IPF) map (Fig. 8(e)).

#### 3.5.2. Effect of temperature on microstructure evolution

High temperature deformation is a thermally activated process where temperature plays a major role in refining the microstructure. In order to study the temperature dependence of microstructure evolution, samples were deformed at four different temperatures (1298, 1348, 1398, and 1448 K) and at  $0.1 \text{ s}^{-1}$  strain rate. Fig. 9 shows an inverse pole figure (IPF) map of sample deformed at temperature of 1298, 1348, 1398, and 1448 K and a strain rate of  $0.1 \text{ s}^{-1}$ . At the lowest temperature

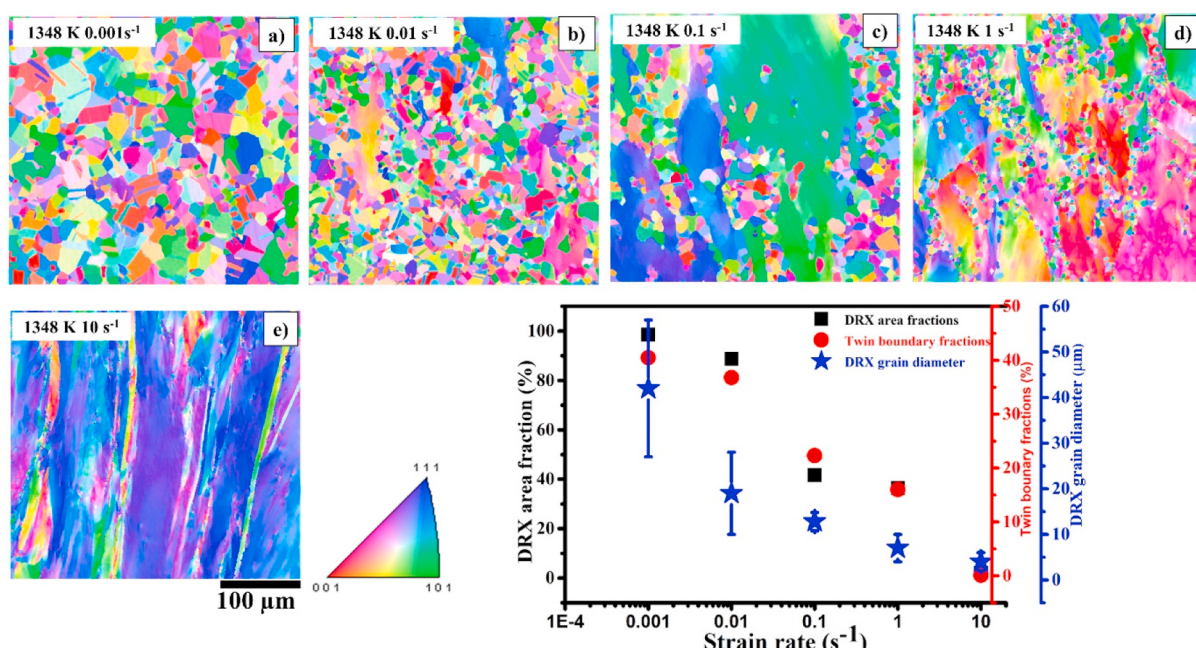


**Fig. 8.** The inverse pole figure (IPF) map (a–e) of Co10Al2Nb alloy deformed at temperature 1348 K and strain rate ranging from  $0.001\text{--}10 \text{ s}^{-1}$ . The graph plot shows the variation of dynamic recrystallization (DRX) grain size, twin boundary fraction, and dynamic recrystallization (DRX) grain fraction.

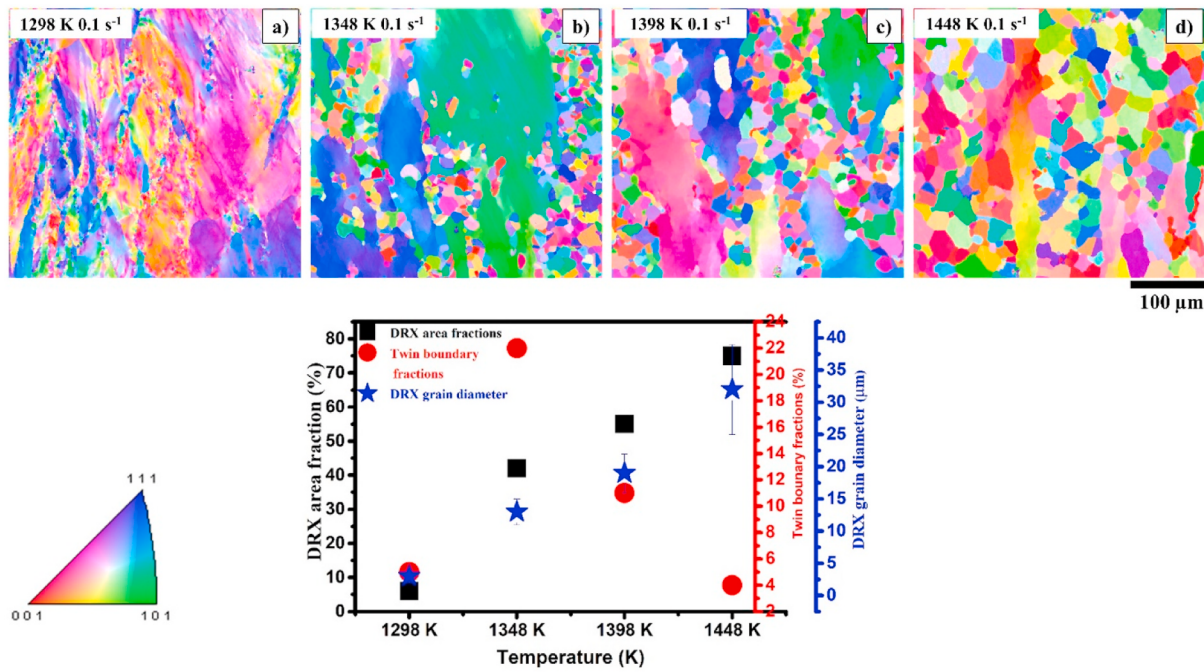


**Fig. 9.** The IPF map (a-d) of Co10Al2Nb alloy deformed at strain rate  $0.1 \text{ s}^{-1}$  and temperature ranging from 1298–1448 K. The graph plot shows the variation of dynamic recrystallization (DRX) grain size, twin boundary fraction, and dynamic recrystallization (DRX) grain fraction.

1298 K, the microstructure primarily consisted of deformed grains and fine dynamic recrystallization (DRX) grains at the grain boundary, as shown in Fig. 9(a). As the temperature further increased to 1348 K and 1398 K, the deformed sample exhibited a partially recrystallized

microstructure consisted of deformed grains, dynamic recrystallization (DRX) grains, and twin boundary ( $\Sigma_3$  boundaries), as shown in Fig. 9 (b & c). At the highest temperature of 1448 K, the deformed sample exhibited a partially recrystallized microstructure with a higher fraction

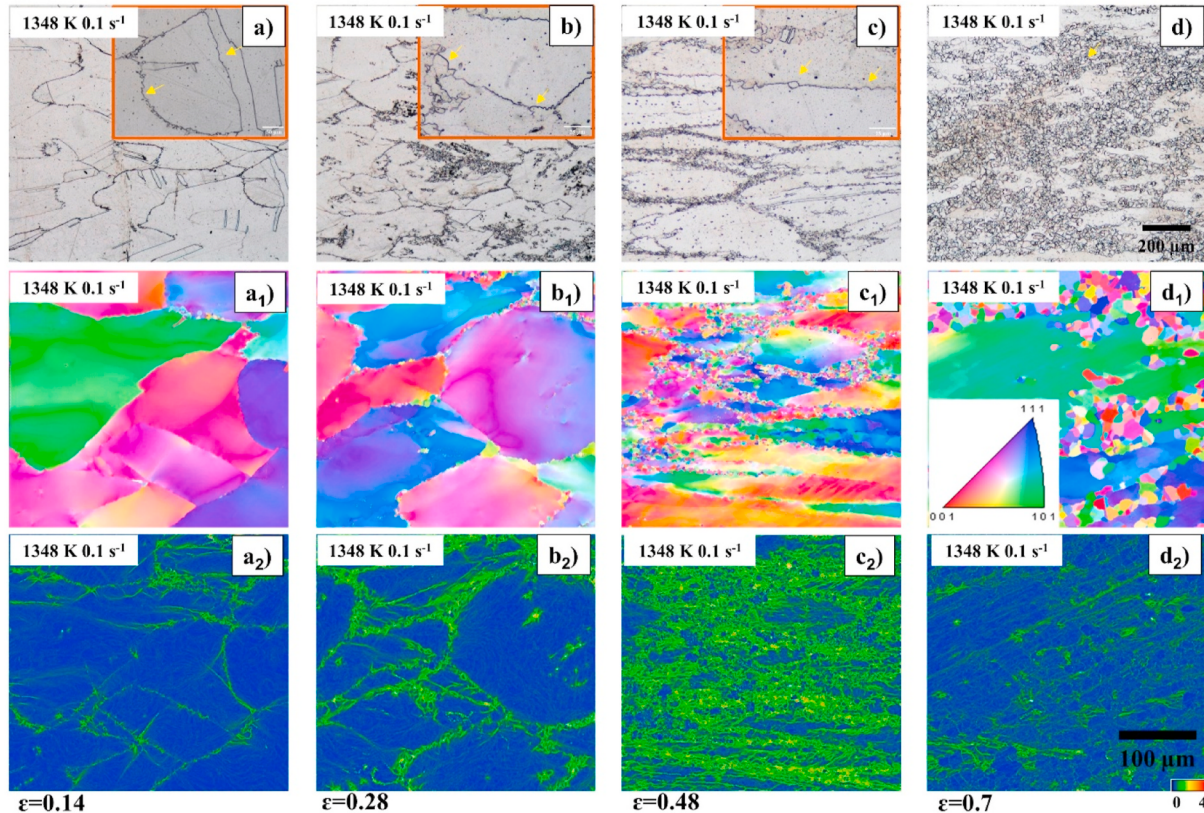


**Fig. 10.** Optical micrograph (a-d), corresponding inverse pole figure (IPF) map (a<sub>1</sub>-d<sub>1</sub>), and kernel average misorientation (KAM) map (a<sub>2</sub>-d<sub>2</sub>) of Co10Al2Nb alloy deformed at strain rate  $0.1 \text{ s}^{-1}$  and temperature 1348 K to a strain of a) 0.14, b) 0.28, c) 0.48, and d) 0.7.

of dynamic recrystallization (DRX) grains (Fig. 9(d)). The plot is shown in Fig. 9, demonstrates the variation of dynamic recrystallization (DRX) grain size ( $\mu\text{m}$ ), twin boundary ( $\Sigma_3$  boundaries) fraction (%), and dynamic recrystallization (DRX) area fraction (%) with respect to different temperatures. Deformation at the lowest temperature of 1298 K produced an inhomogeneous microstructure with a dynamic recrystallization (DRX) grain size of  $4 \pm 1 \mu\text{m}$ , the area fraction of 6 %, and twin boundary ( $\Sigma_3$  boundaries) fraction of 5 %. At temperature 1348 K, dynamic recrystallization (DRX) grain size, area fraction, and twin boundary ( $\Sigma_3$  boundaries) fraction increased to  $13 \pm 2 \mu\text{m}$ , 42 %, and 22 %, respectively. With further increase in temperature to 1398 K, the dynamic recrystallization (DRX) grain size, and area fraction increased to  $19 \pm 3 \mu\text{m}$ , and 55 %, and twin boundary ( $\Sigma_3$  boundaries) fraction reduced to 11 %. At temperature 1448 K, the dynamic recrystallization (DRX) grain size, and area fraction increased to  $32 \pm 7 \mu\text{m}$ , and 75 %, twin boundary ( $\Sigma_3$  boundaries) fraction reduced to 4 %. It was observed that the fraction and size of dynamic recrystallization (DRX) grains increase with an increase in temperature.

### 3.5.3. Effect of strain-level on microstructure evolution

Strain level influences the final microstructure during high temperature deformation. To study the microstructure evolution at different strain levels, samples were deformed to various strains ( $\varepsilon_1 = 0.14$ ,  $\varepsilon_2 = 0.28$ ,  $\varepsilon_3 = 0.48$ , and  $\varepsilon_4 = 0.7$ ), at a constant temperature of 1348 K, and a strain rate of  $0.1 \text{ s}^{-1}$ . The details of the optical microstructure and the corresponding inverse pole figure (IPF) and kernel average misorientation (KAM) maps at different strain levels are shown in Fig. 10(a-d, a<sub>1</sub>-d<sub>1</sub>, and a<sub>2</sub>-d<sub>2</sub>). A serrated/wavy type grain boundary and fine dynamic recrystallization (DRX) grains along the original grain boundary were observed for the samples subjected to a true strain of 0.14 and 0.28, respectively. At further strain up to  $\sim 0.48$ , the sample showed fine dynamic recrystallization (DRX) grains with a size of  $4 \pm 1 \mu\text{m}$ , and an area fraction of 20 % along with deformed grains shown in Fig. 10(c, & c<sub>1</sub>). Here, the deformed grains were found to be elongated perpendicular to the compression axis. The inset in Fig. 10(c), confirmed the discontinuous dynamic recrystallization (DDRX) mechanism is dominant for the Co10Al2Nb alloy. The dynamic recrystallization (DRX) fraction of 42 % with a dynamic recrystallization (DRX) grain size of  $13 \pm 2 \mu\text{m}$  was observed for the sample deformed to a true strain of 0.7, as shown in Fig. 10(d & d<sub>1</sub>).

## 4. Discussion

### 4.1. Flow behavior

Generation, multiplication, and annihilation of dislocations are thermally activated processes, which occur during high temperature deformation. The increase in stress value with the strain in the initial stages of flow curves, shown in Fig. 2, is due to work hardening, where the generation and multiplication of dislocations dominate over the annihilation. For Co10Al2Nb alloy, after reaching the peak, the flow stress decreasing continuously with strain especially at higher strain rate ( $>1 \text{ s}^{-1}$ ). This is possibly due to the plastic instability. The steady-state flow behavior was observed at lower strain rates ( $<1 \text{ s}^{-1}$ ). The flow stress, after reaching a peak value, was observed to attain a constant value with further straining it is due to the equilibrium between the dislocation generation and the annihilation process. Dynamic recovery (DRV) and Dynamic recrystallization (DRX) are the two softening mechanisms operating during high temperature deformation. Dynamic recovery (DRV) can be described as annihilation and arrangement of dislocations to a low energy configuration, whereas DRX essentially related to the formation of new strain-free grains [50]. The dynamic recovery (DRV) and dynamic recrystallization (DRX) can occur simultaneously and/or independently, depending on the deformation conditions and stacking fault energy (SFE). The nature of the flow curves shown in Fig. 2 is a typical deformation response of low stacking fault

energy (SFE) material [51]. At the initial stage, work hardening is dominant, followed by the restoration/softening process with further deformation. The behavior is consistent with earlier reports observed during the deformation of nickel base superalloys [52–54]. The increase in the flow stress value with an increase in strain rate and decrease in temperature shown in Fig. 3 is mainly due to the dislocation interaction and restoration process. At a higher strain rate, the availability time for the restoration process is insufficient, while a decrease in temperature lowers dynamic recrystallization (DRX) kinetics that results in the high-stress value.

### 4.2. Identification of optimum processing regime

#### 4.2.1. Low strain rate ( $\dot{\varepsilon}=0.001$ to $0.1 \text{ s}^{-1}$ ) regime

Steady-state deformation was observed at low strain rates ( $<0.1 \text{ s}^{-1}$ ) regime for all the temperatures. At lower strain rates (0.001 to  $0.01 \text{ s}^{-1}$ ), peak stress was followed by steady-state stress, here flow softening is weak. At a strain rate of  $0.1 \text{ s}^{-1}$ , peak stress followed by flow softening up to a certain strain, and then a steady-state flow behavior was observed. This behavior is consistent with the low stacking fault energy materials such as nickel base, cobalt base, and copper alloys [18,51,52]. The deformation at low strain rates (0.001 to  $0.1 \text{ s}^{-1}$ ) provides sufficient time for the restoration process, which prevents flow localization due to adiabatic heating. The microstructure at low strain rates (0.001 to  $0.1 \text{ s}^{-1}$ ) is shown in Fig. 5. At lowest strain rate ( $0.001 \text{ s}^{-1}$ ), deformed samples revealed almost fully recrystallized microstructure (Fig. 5(a, f, & k)), whereas at  $0.1 \text{ s}^{-1}$  strain rate, the partially recrystallized microstructure was observed (Fig. 5(c, h, m, & r)). This can be attributed to the availability of time for the restoration process during deformation and due to the coarser initial grains. The coarser dynamic recrystallization (DRX) grains with a size of  $136 \pm 27 \mu\text{m}$  was observed at 1448 K and a strain rate of  $0.001 \text{ s}^{-1}$  shown in Fig. 5(a), which is due to the dynamic recrystallization (DRX) grain growth. The deformation at high temperature increases the grain boundary mobility, and lower strain rate provides sufficient time for grains to grow.

#### 4.2.2. High strain rate ( $\dot{\varepsilon}=1$ to $10 \text{ s}^{-1}$ ) regime

At high strain rates (1 to  $10 \text{ s}^{-1}$ ), work hardening is dominant as compared to flow softening due to insufficient time for the restoration process. After reaching the peak stress (especially at  $10 \text{ s}^{-1}$  strain rate), flow stress decreased continuously with strain for all the temperatures shown in Fig. 2(a-d). This is mainly due to the formation of cracks during the deformation at higher stain rate. The formation of surface cracks after post loading are shown in Fig. S1 (supplementary section). Fig. 5 shows the microstructure of the partial recrystallization, and flow localization features such as grain boundary cracking, cavities and shear bands. The deformation at a strain rate of  $1 \text{ s}^{-1}$  for all the temperatures resulted in a partially recrystallized microstructure as shown in Fig. 5(d, i, n, and s), whereas partial recrystallization along with flow localization features was observed at the highest strain rates of  $10 \text{ s}^{-1}$  for all temperature (Fig. 5(e, j, o, and f)). This difference in this behavior is mainly due to adiabatic heating, the rise of temperature associated with the high strain rate deformation (especially at 10 stain rate), which induces the thermal softening in some regions of the sample. Deforming thermally softened regions requires a lower load as compared to the adjacent regions, which results in localized deformation and formation of shear bands. An alternate possibility may be due to the incipient melting, which weakens the grain boundary and causes grain boundary cracking. Similar behavior is reported in nickel base superalloys during high strain rate deformation [55–57].

### 4.3. Validation of microstructure evolution at different processing domain with strain rate sensitivity ( $m$ ) map

Fig. 4 shows the strain rate sensitivity ( $m$ ) contour map superimposed with instability ( $\xi(\dot{\varepsilon})$ ) map. The contours represent the strain

rate sensitivity ( $m$ ) value at different deformation conditions. The strain rate sensitivity ( $m$ ) value varies from 0.01 to 0.3, depending on deformation condition. The higher strain rate sensitivity ( $m$ ) value represents the homogeneous deformation, generally lower cracking tendency because of sufficient flow capacity [58–61]. The lower strain rate sensitivity ( $m$ ) value represents the flow instability and cracking [62, 63].

Deformation at high strain rates ( $10 \text{ s}^{-1}$ ), lower  $m$  value (0.01 to 0.1) was observed for all test temperatures, which also falls under instability region ( $\xi(\dot{\epsilon}) < 0$ ). This indicates the occurrence of flow instabilities during deformation. This region should be avoided during hot forming. On the other hand, deformation at strain rates of 0.001 to  $1 \text{ s}^{-1}$ ,  $m$  value varies with 0.15 to 0.3 depending on deformation conditions. It also falls under stable region ( $\xi(\dot{\epsilon}) > 0$ ). The region is suitable for hot forming. The high  $m$  value of 0.23 to 0.32 was found at medium strain rates ( $0.05$  to  $0.1 \text{ s}^{-1}$ ) for all test temperatures, which indicates the refinement of the microstructure due to the DRX process. From the above discussion, it is established that there is a wide thermomechanical processing window ( $1298\text{--}1448 \text{ K}$ ,  $\leq 0.1 \text{ s}^{-1}$ ) for present alloy which is validated from both processing map and the evolution of deformed microstructure.

#### 4.4. Effect of strain rate on the microstructure evolution

Deformation at different strain rates resulted in the formation of fully recrystallized, partially recrystallized (dynamic recrystallization (DRX) grains along with deformed grains), and only deformed grains shown in Fig. 8(a–e). This difference in the microstructure evolution at different strain rates is mainly due to the difference in the critical plastic strain required for dynamic recrystallization (DRX) grains to nucleate. During high-temperature deformation, the critical plastic strain reduces with a decrease in strain rate [64,65]. Roberts and Ahlbom [66] proposed a criterion for the dynamic recrystallization (DRX) nucleation in terms of critical dislocation density ( $\rho_m$ ) and strain rate ( $\dot{\epsilon}$ ):

$$\frac{\rho_m^3}{\dot{\epsilon}} > \frac{2\gamma_b}{KMLGb^5} \quad [3]$$

where,  $\gamma_b$  and  $M$  represents the grain boundary energy and mobility, respectively.  $L$ ,  $b$ , and  $G$  are the dislocation mean free path, burgers vector of dislocation, and shear modulus and  $K$  is a constant. From equation [3], it is clear that, for a given temperature, a low value of  $\rho_m$  (critical strain) results in nucleation of dynamic recrystallization (DRX) grain at a lower strain rate condition. The dislocation density/critical strain required for dynamic recrystallization (DRX) grains to nucleate increases with an increase in strain rate. In addition, deformation at a lower strain rate gives ample time for dynamic recrystallization (DRX) grains to nucleate and to grow. As a result, fine equiaxed and an increased fraction of dynamic recrystallization (DRX) grains were observed in the low strain rate domain ( $0.1$  to  $0.001 \text{ s}^{-1}$ ) as shown in Fig. 8 (a–c). It was also observed that except for the sample deformed at strain rate  $10 \text{ s}^{-1}$ , all the other samples exhibited flow softening. The area fraction and size of dynamic recrystallization (DRX) grains increase with a decrease in the strain rate as shown in Fig. 8. At a strain rate of  $10 \text{ s}^{-1}$ , there is no sign of dynamic recrystallization (DRX) formation, which is due to the insufficient time to accelerate dynamic recrystallization (DRX) kinetics. The dynamic recrystallization (DRX) grain size decreases with an increase in strain rate. It was found that dynamic recrystallization (DRX) grain size is  $42 \pm 15 \mu\text{m}$  at a strain rate of  $0.001 \text{ s}^{-1}$ , while it reduces to  $7 \pm 3 \mu\text{m}$  at  $1 \text{ s}^{-1}$ . A similar trend is observed in the case of dynamic recrystallization (DRX) area fraction. The above results validate the criteria for the formation of dynamic recrystallization (DRX) given in equation [3]. The increase in twin boundary ( $\Sigma_3$  boundary) fraction with decreasing strain rate shown in the plot (Fig. 8) is mainly due to the sufficient availability of time for grain boundary mobility, which results the nucleation of twins near the original grain boundaries [67].

#### 4.5. Effect of temperature on the microstructure evolution

The nucleation and growth of dynamic recrystallization (DRX) grains mainly depend on the deformation temperature. Fig. 9(a–d) shows the dependence of dynamic recrystallization (DRX) microstructure evolution at different temperatures. The difference in the microstructure evolution at various temperatures is due to a change in the amount of stored energy. It is related to the criteria developed by Roberts and Ahlbom [66]. The factor  $M$  in the equation [3] can be expressed as an Arrhenius type of equation.

$$M = M_0 \exp\left(\frac{-Q_m}{RT}\right) \quad [4]$$

where,  $M_0$  and  $Q_m$  represent the material constant, and the activation energy of grain boundary mobility, respectively.  $R$  is the universal gas constant ( $8.314 \text{ J mol K}^{-1}$ ), and  $T$  is the temperature in K.

Equation [3,4] gives the dependence of dynamic recrystallization (DRX) grains evolution with respect to temperature. The deformation at higher temperatures increases the dynamic recrystallization (DRX) grain fraction and size as shown in Fig. 9(a–d). It is mainly due to the increase in grain boundary migration with the temperature and reduced critical dislocation density for dynamic recrystallization (DRX) nucleation at higher temperatures [68]. As a result, the size and fraction of dynamic recrystallization (DRX) grains are larger at  $1448 \text{ K}$  compared to other deformation temperatures. Twin boundary fraction increased as the deformation temperature increased from  $1298 \text{ K}$  to  $1348 \text{ K}$ . With further increase in deformation temperature to  $1448 \text{ K}$ , the fraction of twin boundary decreases from 22 to 4 % as shown in the plot shown in Fig. 9. This behavior can be attributed to the faster rate of grain boundary migration at  $1448 \text{ K}$  as compared to  $1348 \text{ K}$ . As reported by Harton et al. [69] and Mandol et al. [67] there are two possible reasons for the decrease in twin boundary fractions: 1) At higher temperatures, the faster rate of grain boundary migration results in the reduction of total interfacial energy by reducing grain boundary area and which is more energetically favorable than twining. 2) The insufficient time to nucleate twins due to the faster rate of grain boundary migration at  $1448 \text{ K}$  as compared to  $1348 \text{ K}$ .

#### 4.6. Effect of degree of deformation on the microstructure evolution

Fig. 10(a-d, a<sub>1</sub>-d<sub>1</sub>, and a<sub>2</sub>-d<sub>2</sub>) shows the important role of strain on microstructure evolution during high temperature deformation. The dislocation density/strain energy increases with plastic strain and after reaching a critical strain, which accelerates the dynamic recrystallization (DRX) kinetics. The dynamic recrystallization (DRX) grains nucleates when the applied plastic strain satisfies the condition given in equation [3]. The term  $\frac{2\gamma_b}{KMLGb^5}$  in the equation [3] is mostly independent of deformation conditions (temperature), and the value remains nearly constant for the alloy during deformation [70]. This indicates that dislocation density/stored energy is mainly dependent on applied strain, and value increases with the increase in applied plastic strain.

In polycrystalline materials, as the deformation progress, the accumulation of dislocations near the grain boundary increases. It is mainly due to the incompatibility between the adjacent grains. The gradient in dislocation density close to the grain boundary results in the serrated/wavy type grain boundary, as shown in both optical micrographs Fig. 10 (a), and kernel average misorientation (KAM) map Fig. 10(a<sub>2</sub>), at the initial deformation level ( $\epsilon_1 = 0.14$ ). A serration along the twin boundary can also be noticed in both the optical microscope (OM) image (Fig. 10(a)) and inverse pole figure (IPF) map (Fig. 10a<sub>1</sub>), at  $\epsilon_1 = 0.14$  strain. Here the interface energy of coherent twin boundary is less as compared to the high angle grain boundary. Therefore, twins are energetically less favored for nucleation of new strain-free grains. However, as the deformation progress, the dislocation accumulation increases, which alters the original properties of twins and results in nucleation of

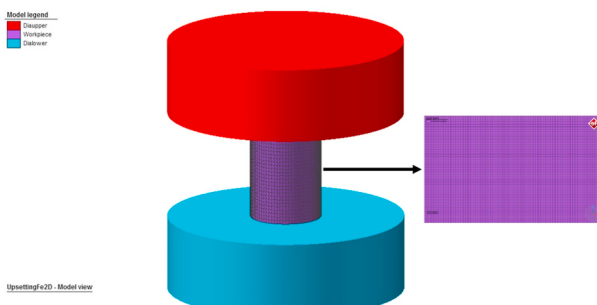


**Fig. 11.** Geometry used for finite element method (FEM) simulation.

the new strain-free grains [71]. As the strain increased to  $\varepsilon_1 = 0.28$ , the fine recrystallized grains are formed along the original grain boundary, which is due to the higher applied strain than the peak strain. When strain level increases to  $\varepsilon_3 = 0.48$ , microstructure consisted of high dislocation density and higher fractions of strain-free grains, as shown in Fig. 10 (c, c<sub>1</sub>, and c<sub>2</sub>). In the above condition, the heterogeneity in the microstructure (both heavily deformed grains oriented perpendicular to compression axis and fine dynamic recrystallization (DRX) grains along the grain boundary) was observed. At strain level  $\varepsilon_4 = 0.7$ , steady-state is the dominant process, here we can see the recrystallized grains along the grain boundary, as shown in Fig. 10 (d, d<sub>1</sub>, and d<sub>2</sub>).

#### 4.7. Finite element method (FEM) simulation and its correlation with microstructure evolution

The material experiences different values of temperature, strain, and strain rate at different locations during the uniaxial high temperature compression tests. To study the distribution of these deformation parameters, hot compression tests were simulated using the finite element method (FEM) simulation package. The geometry used for simulation is shown in Fig. 11.

The effective strain field distribution simulated for samples deformed to 50 % at three different temperatures (1348, 1398, and 1448 K) and a strain rate of 0.1 s<sup>-1</sup> is shown in Fig. 12(a–c). It is observed that the sample experienced a heterogeneous strain field distribution. The center region of the deformed sample experienced higher strain compared to an adjacent area, and the strain is nearly zero at the contact area between the sample and the anvil due to friction. Further, the inhomogeneity in the distribution of strain at a temperature of 1348 K became uniform as

the deformation temperature increased to 1398, and 1448 K, respectively, as shown in Fig. 12 (a–c). To validate the above observations, macro images of the experimentally deformed samples were taken corresponding to the simulated deformation conditions and are shown in Fig. 12(a<sub>1</sub>–c<sub>1</sub>). Deformation at a lower temperature (1348 K) caused the inhomogeneity in the dynamic recrystallization (DRX) microstructure, and as the temperature increased (1398, 1448 K) a uniform distribution of dynamic recrystallization (DRX) grains can be observed. For all three temperatures, the dynamic recrystallization (DRX) fraction at centre region was higher than the adjacent region due to the accumulation of more strain at the center region. The dynamic recrystallization (DRX) fraction and grain size is 42 % and 13±2 μm at 1348 K, and which increased to 55 % and 19±3 μm at 1398 K. When the temperature increased to 1448 K, the dynamic recrystallization (DRX) fraction and grain size increased to 75 % and 32±7 μm, respectively. Thus, the finite element method (FEM) simulation results explain the microstructural observations at various locations of the deformed sample and correlated with the effect of strain on the dynamic recrystallization (DRX) microstructure evolution.

#### 5. Conclusions

The microstructure evolution of newly developed  $\gamma'$  strengthened cobalt base superalloy with a nominal composition of Co-30Ni-10Al-2Nb-4Ti-12Cr (at. %) was studied in a temperature range of 1298–1448 K and strain rate range of 0.001–10 s<sup>-1</sup> through isothermal uniaxial compression tests. Following conclusions are drawn from the present study:

- 1) The Co10Al2Nb alloy shows a hot deformation behavior that is strongly dependent on temperature and strain rate. The flow stress value at any strain increases with decreasing temperature and increases with increasing the strain rate.
- 2) Flow curves and the microstructure evolution of the deformed samples at different conditions revealed that dynamic recrystallization (DRX) is the dominant restoration process.
- 3) Deformed samples exhibited dynamic recrystallization (DRX) microstructure at low strain rate regime (0.001–0.1 s<sup>-1</sup>) and flow localization at high strain rate regime especially at 10 s<sup>-1</sup> for all temperatures.
- 4) Strain rate sensitivity (m) map along with instability ( $\xi(\dot{\varepsilon})$ ) map obtained in this work exhibited two distinct domains: the domain

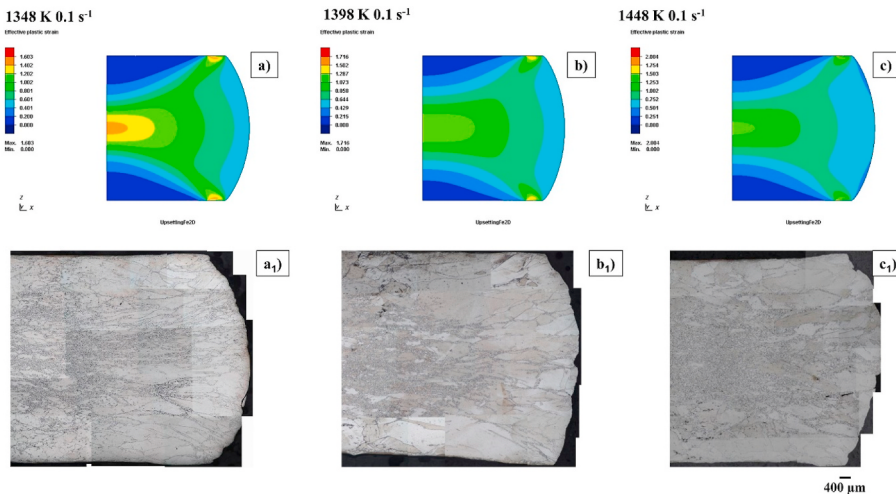


**Fig. 12.** The effective strain field distribution obtained from the finite element method (FEM) simulation (a–c) and corresponding dynamic recrystallization (DRX) microstructure evolution (a<sub>1</sub>–c<sub>1</sub>) obtained from experiment for a deformation at (a), & (a<sub>1</sub>) 0.1 s<sup>-1</sup> strain rate and at temperature 1348 K, (b), & (b<sub>1</sub>) 0.1 s<sup>-1</sup> strain rate and at temperature 1398 K, (c), & (c<sub>1</sub>) 0.1 s<sup>-1</sup> strain rate and at temperature 1448 K.

- The  $m \sim 0.15$  to 0.3, can be seen at strain rate  $0.001\text{--}1\text{ s}^{-1}$  for all the deformation temperatures and it also falls under stable domain ( $\xi(\dot{\varepsilon}) > 0$ ) - here dynamic recrystallization is the dominant restoration process
  - The other domain  $m < 0.13$ , can be observed at strain rate  $>1\text{ s}^{-1}$  for all test temperatures and it falls under unstable domain( $\xi(\dot{\varepsilon}) < 0$ ) -here flow localization was observed and should be avoided during thermomechanical processing
- 5) The microstructure evolution at different strains revealed that discontinuous dynamic recrystallization (DDRX) is the dominant restoration mechanism for the present alloy.
- 6) Dynamic recrystallization (DRX) grains distribution tends to become more homogeneous across various locations as the deformation temperature increased from 1348 to 1448 K. This can be confirmed through finite element method (FEM) simulation (strain field distribution), and the microstructure evolution.

## Declaration of competing interest

The authors declare that they have no known competing financial interests or personal relationships that could have appeared to influence the work reported in this paper.

## CRediT authorship contribution statement

**Nithin Baler:** Conceptualization, Investigation, Methodology, Writing - original draft. **Prafull Pandey:** Investigation, Writing - review & editing. **Kamano Chattopadhyay:** Supervision, Funding acquisition, Writing - review & editing. **Gandham Phanikumar:** Supervision, Funding acquisition, Writing - review & editing.

## Acknowledgement

All authors acknowledge the thermo-mechanical simulation Gleble 3800® facility at IIT Madras funded by DST-FIST (Department of Science and Technology, Govt. of India) program. Financial support from the GTMAP programme of Aeronautical Research and Development Board, Govt. of India is gratefully acknowledged. The authors also thank Prof. Satyam Suwas, Department of Materials Engineering, IISc Bengaluru for his valuable suggestions.

## Appendix A. Supplementary data

Supplementary data to this article can be found online at <https://doi.org/10.1016/j.msea.2020.139498>.

## References

- [1] R.C. Reed, The Superalloys: Fundamentals and Applications, Cambridge University Press, 2006, <https://doi.org/10.1017/CBO9780511541285>.
- [2] T.M. Pollock, A.S. Argon, Creep resistance of CMSX-3 nickel base superalloy single crystals, *Acta Metall. Mater.* 40 (1992) 1–30, [https://doi.org/10.1016/0956-7151\(92\)90195-K](https://doi.org/10.1016/0956-7151(92)90195-K).
- [3] J.H. Perezko, The hotter the engine, the better, *Science* 326 (2009) 1068–1069, <https://doi.org/10.1126/science.1179327>.
- [4] Sato Junishi Kiyohito, Kainuma Ryosuke, Oikawa Katunari, Ohnuma Ikuo, Cobalt-base alloy with high heat resistance and high strength and process for producing the same, US PATENT (2008) US20080185078.
- [5] S.K. Makineni, B. Nithin, K. Chattopadhyay, Gamma-gamma prime strengthened tungsten free cobalt-based superalloy, Indian Patent (2014). Application number 1981/CHE/2014.
- [6] Katsushi Tanaka, Masahiro Ooshima, Nobuyasu Tsuno, Akihiro Sato, Haruyuki Inui, Creep deformation of single crystals of newCo-Al-W-based alloys with fcc/L12 two-phasicmicrostructures, *Phil Mag* 92 (2012) 4011–4027. <https://doi.org/10.1080/14786435.2012.700416>.
- [7] M.S. Titus, A. Suzuki, T.M. Pollock, Creep and directional coarsening in single crystals of new  $\gamma\text{-}\gamma'$  cobalt-base alloys, *Scripta Mater.* 66 (2012) 574–577, <https://doi.org/10.1016/j.scriptamat.2012.01.008>.
- [8] M. Titus, A. Suzuki, T. Pollock, High Temperature Creep of New L12 Containing Cobalt-Base Superalloys, *SUPERALLOYS* (2012) 110, <https://doi.org/10.1002/9781118516430.ch91>. Wiley.
- [9] T.M. Pollock, J. Dibbern, M. Tsunekane, J. Zhu, A. Suzuki, New Co-based  $\gamma\text{-}\gamma'$  high-temperature alloys, *JOM* 62 (2010) 58–63, <https://doi.org/10.1007/s11837-010-0013-y>.
- [10] J. Koßmann, C.H. Zenk, I. Lopez-Galilea, S. Neumeier, A. Kostka, S. Huth, W. Theisen, M. Göken, R. Drautz, T. Hammerschmidt, Microsegregation and precipitates of an as-cast Co-based superalloy—microstructural characterization and phase stability modelling, *J. Mater. Sci.* 50 (2015) 6329–6338, <https://doi.org/10.1007/s10853-015-9177-8>.
- [11] A.K. Misra, Corrosion of metals and alloys in sulfate melts at 750°C, *Oxid Met* 25 (1986) 373–396, <https://doi.org/10.1007/BF01072916>.
- [12] David Furrer, Hans Fecht, Ni-Based Superalloys for Turbine Discs, *JOM* 51 (1999) 14–17, <https://doi.org/10.1007/s11837-999-0005-y>.
- [13] K. Sahitya, I. Balasundar, P. Pant, T. Raghu, H.K. Nandi, V. Singh, P. Ghosal, M. Ramakrishna, Deformation behaviour of an as-cast nickel base superalloy during primary hot working above and below the gamma prime solvus, *Mater. Sci. Eng., A* (2019), <https://doi.org/10.1016/j.msea.2019.03.083>.
- [14] A.J. Brand, K. Karhausen, R. Kopp, Microstructural simulation of nickel base alloy Inconel® 718 in production of turbine discs, *Mater. Sci. Technol.* 12 (1996) 963–969, <https://doi.org/10.1179/mst.1996.12.11.963>.
- [15] Y. Wang, W.Z. Shao, L. Zhen, L. Yang, X.M. Zhang, Flow behavior and microstructures of superalloy 718 during high temperature deformation, *Mater. Sci. Eng., A* 497 (2008) 479–486, <https://doi.org/10.1016/j.msea.2008.07.046>.
- [16] S.L. Semiatin, J.M. Shank, A.R. Shiveley, W.M. Saurber, E.F. Gaussa, A.L. Pilchak, The effect of forging variables on the supersolvus heat-treatment response of powder-metallurgy nickel-base superalloys, *Metall. Mater. Trans.* 45 (2014) 6231–6251, <https://doi.org/10.1007/s11661-014-2572-y>.
- [17] V. Anil Kumar, R.K. Gupta, S.V.S. Narayana Murty, A.D. Prasad, Hot workability and microstructure control in Co20Cr15W10Ni cobalt-based superalloy, *J. Alloys Compd.* 676 (2016) 527–541, <https://doi.org/10.1016/j.jallcom.2016.03.186>.
- [18] J. Favre, Y. Koizumi, A. Chiba, D. Fabregue, E. Maire, Deformation behavior and dynamic recrystallization of biomedical Co-Cr-W-Ni (L-605) alloy, *Metall. Mater. Trans.* 44 (2013) 2819–2830, <https://doi.org/10.1007/s11661-012-1602-x>.
- [19] K. Yamanaka, M. Mori, K. Kuramoto, A. Chiba, Development of new Co-Cr-W-based biomedical alloys: effects of microalloying and thermomechanical processing on microstructures and mechanical properties, *Mater. Des.* 55 (2014) 987–998, <https://doi.org/10.1016/j.matdes.2013.10.052>.
- [20] K. Yamanaka, M. Mori, A. Chiba, Dynamic recrystallization of a biomedical Co-Cr-W-based alloy under hot deformation, *Mater. Sci. Eng., A* 592 (2014) 173–181, <https://doi.org/10.1016/j.msea.2013.11.002>.
- [21] J. Sato, Cobalt-base high-temperature alloys, *Science* 312 (2006) 90–91, <https://doi.org/10.1126/science.1121738>.
- [22] Kazuya Shinagawa, Toshihiro Omori, Katsunari Oikawa, Ryosuke Kainuma, Kiyohto Ishida, Ductility enhancement by boron addition in Co-Al-W high-temperature alloys, *Scripta Mater.* 61 (2009) 612–615, <https://doi.org/10.1016/j.scriptamat.2009.05.037>.
- [23] A. Suzuki, T.M. Pollock, High-temperature strength and deformation of  $\gamma\text{-}\gamma'$  two-phase Co-Al-W-base alloys, *Acta Mater.* 56 (2008) 1288–1297, <https://doi.org/10.1016/j.actamat.2007.11.014>.
- [24] S.K. Makineni, A. Samanta, T. Rojhirunsakool, T. Alam, B. Nithin, A.K. Singh, R. Banerjee, K. Chattopadhyay, A new class of high strength high temperature Cobalt based  $\gamma\text{-}\gamma'$  Co-Mo-Al alloys stabilized with Ta addition, *Acta Mater.* 97 (2015) 29–40, <https://doi.org/10.1016/j.actamat.2015.06.034>.
- [25] S.K. Makineni, B. Nithin, K. Chattopadhyay, A new tungsten-free  $\gamma\text{-}\gamma'$  Co-Al-Mo-Nb-based superalloy, *Scripta Mater.* 98 (2015) 36–39, <https://doi.org/10.1016/j.scriptamat.2014.11.009>.
- [26] S.K. Makineni, B. Nithin, K. Chattopadhyay, Synthesis of a new tungsten-free  $\gamma\text{-}\gamma'$  cobalt-based superalloy by tuning alloying additions, *Acta Mater.* 85 (2015) 85–94, <https://doi.org/10.1016/j.actamat.2014.11.016>.
- [27] P.J. Bocchini, C.K. Sudbrack, D.J. Sauza, R.D. Noebe, D.N. Seidman, D.C. Dunand, Effect of tungsten concentration on microstructures of Co-10Ni-6Al-(0,2,4,6)W-6Ti (at. %) cobalt-based superalloys, *Mater. Sci. Eng., A* (2017), <https://doi.org/10.1016/j.msea.2017.06.018>.
- [28] D.J. Sauza, P.J. Bocchini, D.C. Dunand, D.N. Seidman, Influence of ruthenium on microstructural evolution in a model Co-Al-W superalloy, *Acta Mater.* 117 (2016) 135–145, <https://doi.org/10.1016/j.actamat.2016.07.014>.
- [29] E.A. Lass, D.J. Sauza, D.C. Dunand, D.N. Seidman, Multicomponent  $\gamma'$ -strengthened Co-based superalloys with increased solvus temperatures and reduced mass densities, *Acta Mater.* 147 (2018) 284–295, <https://doi.org/10.1016/j.actamat.2018.01.034>.
- [30] A. Bauer, S. Neumeier, F. Pyckzak, R.F. Singer, M. Göken, Creep properties of different  $\gamma'$ -strengthened Co-base superalloys, *Mater. Sci. Eng., A* 550 (2012) 333–341, <https://doi.org/10.1016/j.msea.2012.04.083>.
- [31] G. Feng, H. Li, S.S. Li, J.B. Sha, Effect of Mo additions on microstructure and tensile behavior of a Co-Al-W-Ta-B alloy at room temperature, *Scripta Mater.* 67 (2012) 499–502, <https://doi.org/10.1016/j.scriptamat.2012.06.013>.
- [32] I. Povstugar, C.H. Zenk, R. Li, P. Choi, S. Neumeier, O. Dolotko, M. Hoelzel, M. Göken, D. Raabe, Elemental partitioning, lattice misfit and creep behaviour of Cr containing  $\gamma'$  strengthened Co base superalloys, *Materials Science and Technology* 32 (2016) 220–225, <https://doi.org/10.1179/1743284715Y.0000000112>.
- [33] D.J. Sauza, D.C. Dunand, R.D. Noebe, D.N. Seidman,  $\gamma'$ -(L12) precipitate evolution during isothermal aging of a Co-Al-W-Ni superalloy, *Acta Mater.* 164 (2019) 654–662, <https://doi.org/10.1016/j.actamat.2018.11.014>.
- [34] S. Meher, H.-Y. Yan, S. Nag, D. Dye, R. Banerjee, Solute partitioning and site preference in  $\gamma\text{-}\gamma'$  cobalt-base alloys, *Scripta Mater.* 67 (2012) 850–853, <https://doi.org/10.1016/j.scriptamat.2012.08.006>.

- [35] L.P. Freund, S. Giese, D. Schwimmer, H.W. Höppel, S. Neumeier, M. Göken, High temperature properties and fatigue strength of novel wrought  $\gamma/\gamma'$  Co-base superalloys, *J. Mater. Res.* 32 (2017) 4475–4482, <https://doi.org/10.1557/jmr.2017.315>.
- [36] S. Neumeier, L.P. Freund, M. Göken, Novel wrought  $\gamma/\gamma'$  cobalt base superalloys with high strength and improved oxidation resistance, *Scripta Mater.* 109 (2015) 104–107, <https://doi.org/10.1016/j.scriptamat.2015.07.030>.
- [37] E.T. McDevitt, Vacuum induction melting and vacuum arc remelting of Co-Al-W-X gamma-prime superalloys, in: MATEC Web of Conferences 14, 2014, <https://doi.org/10.1051/matecconf/20141402001>, 02001.
- [38] S.A. Sani, H. Arabi, G.R. Ebrahimi, Hot deformation behavior and DRX mechanism in a  $\gamma/\gamma'$ -cobalt-based superalloy, *Mater. Sci. Eng.* 764 (2019) 138165, <https://doi.org/10.1016/j.msea.2019.138165>.
- [39] S.K. Makineni, B. Nithin, D. Palanisamy, K. Chattopadhyay, Phase evolution and crystallography of precipitates during decomposition of new “tungsten-free” Co (Ni)-Mo-Al-Nb  $\gamma/\gamma'$  superalloys at elevated temperatures, *J. Mater. Sci.* 51 (2016) 7843–7860, <https://doi.org/10.1007/s10853-016-0026-1>.
- [40] B. Nithin, A. Samanta, S.K. Makineni, T. Alam, P. Pandey, A.K. Singh, R. Banerjee, K. Chattopadhyay, Effect of Cr addition on  $\gamma/\gamma'$  cobalt-based Co-Mo-Al-Ta class of superalloys: a combined experimental and computational study, *J. Mater. Sci.* 52 (2017) 11036–11047, <https://doi.org/10.1007/s10853-017-1159-6>.
- [41] P. Pandey, S.K. Makineni, A. Samanta, A. Sharma, S.M. Das, B. Nithin, C. Srivastava, A.K. Singh, D. Raabe, B. Gault, K. Chattopadhyay, Elemental site occupancy in the L12 A3B ordered intermetallic phase in Co-based superalloys and its influence on the microstructure, *Acta Mater.* 163 (2019) 140–153, <https://doi.org/10.1016/j.actamat.2018.09.049>.
- [42] S.M. Das, M.P. Singh, K. Chattopadhyay, Evolution of oxides and their microstructures at 800°C in a  $\gamma$ -stabilised Co-Ni-Al-Mo-Ta superalloy, *Corrosion Sci.* 155 (2019) 46–54, <https://doi.org/10.1016/j.corsci.2019.02.013>.
- [43] P. Pandey, A.K. Sawant, B. Nithin, Z. Peng, S.K. Makineni, B. Gault, K. Chattopadhyay, On the effect of Re addition on microstructural evolution of a CoNi-based superalloy, *Acta Mater.* 168 (2019) 37–51, <https://doi.org/10.1016/j.actamat.2019.01.046>.
- [44] N. Baler, P. Pandey, D. Palanisamy, S.K. Makineni, G. Phanikumar, K. Chattopadhyay, On the effect of W addition on microstructural evolution and  $\gamma'$  precipitate coarsening in a Co-30Ni-10Al-5Mo-2Ta-2Ti alloy, *Materialia*, <https://doi.org/10.1016/j.mtla.2020.100632>, 2020, 100632.
- [45] B. Nithin, K. Chattopadhyay, G. Phanikumar, Characterization of the hot deformation behavior and microstructure evolution of a new  $\gamma/\gamma'$  strengthened cobalt-based superalloy, *Metall. Mater. Trans.* 49 (2018) 4895–4905, <https://doi.org/10.1007/s11661-018-4795-9>.
- [46] Prafull Pandey, On the Development of Low Mass Density  $\gamma'$  Strengthened Co Based Superalloys, IISc Bangalore, 2019.
- [47] Prafull Pandey, Majumdar Namrata, Sharma Abhishek, Palanisamy Dhanalakshmi, Sharma Amit, Singh Mahander, Patil Chaitali, Baler Nithin, Makineni Surendra, Dipankar Banerjee, Kamano Chattopadhyay, Towards the Development of Low Density  $\gamma/\gamma'$  Misfit CoNi-Base Superalloys with Promising High Temperature Mechanical Properties, *Acta Materialia* (2020). Submitted for publication.
- [48] Mechanical Metallurgy Dieter, 1988. ISBN 0-07-100406-8.
- [49] H. Ziegler, I.N. Sneddon, R. Hill (Eds.), *Progress in Solid Mechanics*, vol. 4, Wiley, New York, 1963, pp. 63–193.
- [50] T. Sakai, A. Belyakov, R. Kaibyshev, H. Miura, J.J. Jonas, Dynamic and post-dynamic recrystallization under hot, cold and severe plastic deformation conditions, *Prog. Mater. Sci.* 60 (2014) 130–207, <https://doi.org/10.1016/j.pmatsci.2013.09.002>.
- [51] H. Zhang, H. Zhang, L. Li, Hot deformation behavior of Cu-Fe-P alloys during compression at elevated temperatures, *J. Mater. Process. Technol.* 209 (2009) 2892–2896, <https://doi.org/10.1016/j.jmatprotec.2008.06.048>.
- [52] K.A. Babu, S. Mandal, A. Kumar, C.N. Athreya, B. de Boer, V.S. Sarma, Characterization of hot deformation behavior of alloy 617 through kinetic analysis, dynamic material modeling and microstructural studies, *Mater. Sci. Eng., A* 664 (2016) 177–187, <https://doi.org/10.1016/j.msea.2016.04.004>.
- [53] J. Wang, J. Dong, M. Zhang, X. Xie, Hot working characteristics of nickel-base superalloy 740H during compression, *Mater. Sci. Eng., A* 566 (2013) 61–70, <https://doi.org/10.1016/j.msea.2012.12.077>.
- [54] Y. Liu, R. Hu, J. Li, H. Kou, H. Li, H. Chang, H. Fu, Characterization of hot deformation behavior of Haynes230 by using processing maps, *J. Mater. Process. Technol.* 209 (2009) 4020–4026, <https://doi.org/10.1016/j.jmatprotec.2008.09.024>.
- [55] F.-L. Sui, L.-X. Xu, L.-Q. Chen, X.-H. Liu, Processing map for hot working of Inconel 718 alloy, *J. Mater. Process. Technol.* 211 (2011) 433–440, <https://doi.org/10.1016/j.jmatprotec.2010.10.015>.
- [56] S.S. Sathesh Kumar, T. Raghu, Pinaki P. Bhattacharjee, G. Appa Rao, Utpal Borah, Constitutive modeling for predicting peak stress characteristics during hot deformation of hot isostatically processed nickel-base superalloy, *J. Mater. Sci.* 50 (2015) 6444–6456, <https://doi.org/10.1007/s10853-015-9200-0>.
- [57] Y. Wu, Z. Liu, X. Qin, C. Wang, L. Zhou, Effect of initial state on hot deformation and dynamic recrystallization of Ni-Fe based alloy GH94G for steam boiler applications, *J. Alloys Compd.* 795 (2019) 370–384, <https://doi.org/10.1016/j.jallcom.2019.05.022>.
- [58] B. Paul, A. Sarkar, J.K. Chakrabarty, A. Verma, R. Kapoor, A.C. Bidaye, I.G. Sharma, A.K. Suri, Dynamic recrystallization in sintered cobalt during high-temperature deformation, *Metall. Mater. Trans.* 41 (2010) 1474–1482, <https://doi.org/10.1007/s11661-010-0181-y>.
- [59] R. Kapoor, J.K. Chakrabarty, C.C. Gupta, S.L. Wadekar, Characterization of superplastic behaviour in the  $(\alpha+\beta)$  phase field of Zr-2.5wt.%Nb alloy, *Mater. Sci. Eng., A* 392 (2005) 191–202, <https://doi.org/10.1016/j.msea.2004.09.023>.
- [60] A. Chaudhuri, A.N. Behera, A. Sarkar, R. Kapoor, R.K. Ray, S. Suwas, Hot deformation behaviour of Mo-TZM and understanding the restoration processes involved, *Acta Mater.* 164 (2019) 153–164, <https://doi.org/10.1016/j.actamat.2018.10.037>.
- [61] A. Chaudhuri, A. Sarkar, S. Suwas, Investigation of stress-strain response, microstructure and texture of hot deformed pure molybdenum, *Int. J. Refract. Metals Hard Mater.* 73 (2018) 168–182, <https://doi.org/10.1016/j.ijrmhm.2018.02.011>.
- [62] A. Sarkar, R. Kapoor, A. Verma, J.K. Chakrabarty, A.K. Suri, Hot deformation behavior of Nb-1Zr-0.1C alloy in the temperature range 700–1700°C, *J. Nucl. Mater.* 422 (2012) 1–7, <https://doi.org/10.1016/j.jnucmat.2011.11.064>.
- [63] K. Arun Babu, Y.H. Mozumder, R. Saha, S. Mandal, A systematic assessment of various stability/instability criteria in predicting the hot deformation-related instabilities in super-304H stainless steels, *J. Mater. Eng. Perform.* 28 (2019) 4718–4730, <https://doi.org/10.1007/s11665-019-04238-1>.
- [64] M. Shaban, B. Eghbali, Determination of critical conditions for dynamic recrystallization of a microalloyed steel, *Mater. Sci. Eng., A* 527 (2010) 4320–4325, <https://doi.org/10.1016/j.msea.2010.03.086>.
- [65] I. Mejía, A. Bedolla-Jacuinde, C. Maldonado, J.M. Cabrera, Determination of the critical conditions for the initiation of dynamic recrystallization in boron microalloyed steels, *Mater. Sci. Eng., A* 528 (2011) 4133–4140, <https://doi.org/10.1016/j.msea.2011.01.102>.
- [66] W. Roberts, B. Ahlbom, A nucleation criterion for dynamic recrystallization during hot working, *Acta Metall.* 26 (1978) 801–813, [https://doi.org/10.1016/0001-6160\(78\)90030-5](https://doi.org/10.1016/0001-6160(78)90030-5).
- [67] S. Mandal, A.K. Bhaduri, V.S. Sarma, Studies on twinning and grain boundary character distribution during anomalous grain growth in a Ti-modified austenitic stainless steel, *Mater. Sci. Eng., A* 515 (2009) 134–140, <https://doi.org/10.1016/j.msea.2009.02.042>.
- [68] Lin Wen, Dong-Xu, H.-B. Li, X.-M. Chen, J. Deng, L.-T. Li, Hot deformation behavior and processing map of a typical Ni-based superalloy, *Mater. Sci. Eng., A* 591 (2014) 183–192, <https://doi.org/10.1016/j.msea.2013.09.049>.
- [69] D. Horton, C.B. Thomson, V. Randle, Aspects of twinning and grain growth in high purity and commercially pure nickel, *Mater. Sci. Eng., A* 203 (1995) 408–414, [https://doi.org/10.1016/0921-5093\(95\)09821-6](https://doi.org/10.1016/0921-5093(95)09821-6).
- [70] F.J. Humphreys, M. Hatherly, *Recrystallization and Related Annealing Phenomena*, Elsevier, 2012.
- [71] M. Zouari, N. Bozzolo, R.E. Logé, Mean field modelling of dynamic and post-dynamic recrystallization during hot deformation of Inconel 718 in the absence of  $\delta$  phase particles, *Mater. Sci. Eng., A* 655 (2016) 408–424, <https://doi.org/10.1016/j.msea.2015.12.102>.